

---

# 5 Spike-Train Analysis

*Inés Samengo, Daniel Elijah, and Marcelo A. Montemurro*

## CONTENTS

5.1	Introduction .....	75
5.2	Testing the Neural Code with Stochastic Inputs.....	76
5.3	Measuring Spike Train Patterns .....	76
5.3.1	Model of Burst Generation .....	76
5.3.2	ISI Distributions and Correlation Functions.....	78
5.3.3	Autocorrelation Function and Fano Factor .....	79
5.3.4	Tuning Curves for Spike Patterns.....	80
5.3.5	Event Triggered Averages .....	83
5.4	Revealing Intrinsic Dynamical Properties .....	84
5.4.1	Neurons as Dynamical Systems .....	85
5.4.2	Phase-Description of Spiking Neurons .....	87
5.4.3	Phase-Response Curves of Resonator and Integrator Neurons .....	89
5.4.4	Relationship between the Phase-Response Curve and the STA: Supra-Threshold Regime .....	90
5.4.5	Relationship between the Phase-Response Curve and the STA: Sub-Threshold Regime .....	90
5.4.6	Bridging the Two Regimes .....	94
	Summary .....	95
	References.....	95

## 5.1 INTRODUCTION

Spike-train analysis techniques provide an enormously powerful tool to study the neural code. They only require extracellular recordings of a sensory neuron, and a register of the stimulus signal driving the cell. The aim is to understand the way in which the neural response represents the external world.

Over the last few decades significant advance has been attained in the understanding of the role of single spikes in neural coding (Rieke, 1997; Gabbiani and Koch, 1998). Those studies have led to a comprehensive view of the relationship between stimuli and independent spike output. However, neural responses also contain more complex firing patterns structured as collections of correlated spikes (Averbeck et al., 2006). The functional role of those collections, and their relationship to the stimulus cannot be explained in terms of the summation of isolated events. Recent studies (Nadasdy, 2000; Fellous et al., 2004; Nelken et al., 2005; Gütig and Sompolinsky, 2006; Montemurro et al., 2007; Gaudry and Reinagel, 2008; Eyherabide and Samengo, 2010a,b) are now beginning to systematically analyze the functional role of patterns in the neural code.

In principle, spike patterns can be any stereotypical combination of spikes and silences. However, out of all the possible patterns that can be conceived, bursts constitute the most ubiquitous form of pattern found in the nervous system. A large number of neurons are known to be able to generate bursts. In bursting neurons, spikes belonging to one burst are fired in rapid succession, and different bursts are separated by silent periods (Izhikevich, 2007). In this chapter, we review some classical spike-train

analysis techniques originally developed to study simple neural codes, and adapt them to reveal the structure of more complex, pattern-based codes. In particular, we use burst firing as an example of pattern-based codes. However, our results are also applicable to other neural codes, based on more general patterns. In addition, we show that spike-train analysis techniques entirely based on extracellular recordings can be used to disclose intrinsic coding properties of single neurons. These modern procedures, therefore, give insight on the way complex cellular dynamics build up sophisticated neural codes.

## 5.2 TESTING THE NEURAL CODE WITH STOCHASTIC INPUTS

Spike-train analysis techniques aim at extracting information about the neural code by driving a neuron with a stochastic stimulus and studying the statistical properties of the obtained responses. One of the basic assumptions of this approach is that all the relevant information of the neural activity is contained in the sequence of spike times (Dayan and Abbott, 2001). Thus, we explicitly neglect any other information that could, in principle, be contained for example in the shape of individual spikes, and conceive a given neural response as the sequence of spikes times  $S = \{t_i\}_{i=1}^N$  where  $N$  represents the total number of spikes. For notation purposes, it is convenient to represent the spike train as a sequence of Delta functions (Arfken and Weber, 2005)

$$\rho(t) = \sum_{i=0}^N \delta(t - t_i). \quad (5.1)$$

The relevant statistical properties of the spike train can be derived from the function  $\rho(t)$ .

The use of stochastic stimuli is intended to represent the fluctuating input currents processed by a neuron under physiological conditions. Such currents may result from numerous unsynchronized synaptic inputs, in the case of neurons from the central nervous system, or from the transduction of fluctuating sensory stimuli, in the case of peripheral receptors. In simulations, stochastic input currents attempt to represent a rich and variate space of input signals, so as to explore all the possible responses of the cell to time-dependent inputs. Here, we run our simulations with two types of signals. In most cases, we model the input to the neuron by an Ornstein–Uhlenbeck process (Gardiner, 2009) of short correlation time. This type of signal presents amplitudes that are distributed according to a Gaussian and whose successive values are exponentially correlated with a characteristic correlation time. This process is commonly used as a simple model of naturalistic signals. We also use filtered Gaussian noise (see [Figure 5.7](#)), in order for our results to be comparable with earlier studies. The two types of stochastic signals are entirely characterized by their variance and correlation time. They only differ in the shape of the tails of their Fourier transform, but are otherwise both adequate to explore the response of neural models to rich, time-dependent stimuli.

## 5.3 MEASURING SPIKE TRAIN PATTERNS

In this section, we introduce some basic spike-train analysis techniques aiming at characterizing the structure of the neural response. Some of these methods have the advantage that can be applied both to spontaneous and stimulus-evoked activity. Others, instead, are specifically designed to discover patterns in the neural response whose meaning can be interpreted in terms of the stimulus. They can help in building up a dictionary that relates the relevant code words in the neural response (the patterns) to the encoded stimulus (the message).

### 5.3.1 MODEL OF BURST GENERATION

In this chapter, bursts constitute our prototype of spike patterns. There is a large variety of known bursting neurons related to different mechanisms (Izhikevich, 2007). In the first section of this

chapter, we analyze the neural code of bursting neurons, and compare it to that of nonbursting cells. Initially, we work with two simple models, the Integrate-and-Fire (IF) neuron, and the Integrate-and-Fire-or-Burst (IFB) cell (Smith et al., 2000). Each of them constitutes the simplest prototype of a nonbursting and a bursting cell, and several studies have used them to represent real neurons in the brain. Specifically, the IFB model has been used to represent thalamic relay cells. Later on, when studying the neural code of more complex models, we also introduce bursting models representing cortical pyramidal cells.

The IFB model consists of a standard IF neuron with an additional slow variable inactivating a slow threshold  $\text{Ca}^{2+}$  conductance, related to T-type  $\text{Ca}^{2+}$  channels and the associated  $I_T$  current. The equations are

$$C \frac{dV}{dt} = I_{\text{ext}} - I_L - I_T \quad (5.2)$$

$$\frac{dh}{dt} = \begin{cases} -h/\tau_h^- & (V > V_h) \\ (1-h)/\tau_h^+ & (V < V_h) \end{cases} \quad (5.3)$$

In Equation 5.2,  $I_{\text{ext}}$  represents the external stimulus, and  $I_L$  is a leakage current given by  $I_L = g_L(V - V_L)$ . Here,  $g_L$  is the leakage conductance and  $V_L$  is the reversal potential associated with this current. In addition,  $I_T$  is a low-threshold current of the form  $I_T = g_T m_\infty h(V - V_T)$ , where  $m_\infty = H(V - V_h)$  and  $H(x)$  is the Heaviside step function (Arfken and Weber, 2005),  $g_T$  is the maximum conductance associated with the  $I_T$  current,  $V_T$  is the corresponding reversal potential, and  $h$  is the slow variable related to the low-threshold current. Equation 5.3 states that the variable  $h$  decays to zero with a time constant  $\tau_h^-$  when  $V > V_h$ , and tends to one when  $V < V_h$ . A spike is produced whenever the membrane potential crosses a threshold  $V_h$  from below; immediately after firing the membrane potential is reset to  $V_r$ . Details on the behavior of the model under oscillatory input can be found in Smith et al. (2000). By simply eliminating the  $I_T$  current we recover the IF model, which only produces tonic firing (see Figure 5.1).

When the IF and the IFB models are driven with an Ornstein–Uhlenbeck process, they produce the sample spike trains shown in Figure 5.1. The IF model produces an unstructured train of isolated spikes, whereas the IFB neuron generates a sequence of bursts of variable length. The aim of the following sections is to develop a systematic way of recognizing these patterns, and to understand what they represent in terms of the stimulus.

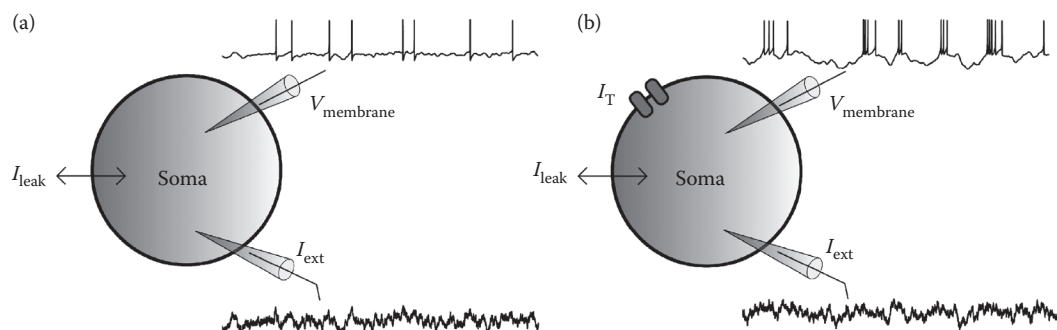


**FIGURE 5.1** Diagram of neuron models displaying tonic and burst firing. A net synaptic input is applied to the neuron (bottom traces) that elicits both sub-threshold and spiking behavior at the soma (top traces). (a) Integrate-and-Fire (IF) neuron model. The typical firing pattern consists of tonic spikes. (b) Integrate-and-Fire-or-Burst neuron model, including a low-threshold current. Bursts are clearly visible as groups of spikes separated by a short interval (typically less than 10 ms).

### 5.3.2 ISI DISTRIBUTIONS AND CORRELATION FUNCTIONS

Of particular importance is the distribution of interspike intervals (ISIs)  $P(\Delta t)$ , where  $\Delta t$  refers to the lapse between two consecutive spikes. This distribution is useful to detect intervals between spikes that are particularly abundant (appearing as peaks) or scarce (as valleys). If spike generation is governed by a Poisson process of uniform rate, then the ISI distribution has an exponential shape. Figure 5.2 shows the ISI distribution for both the tonic (IF) and bursting (IFB) models. In both cases,  $P(\Delta t)$  is strictly zero for  $\Delta t < 3$  ms. Absolute refractoriness prohibits the generation of two spikes too close in time. Therefore, in all minimally realistic model neurons, small ISIs are absent from  $P(\Delta t)$ . The relative refractory period is an interval where spike generation is possible, though unlikely. In this range, one typically observes a rapidly growing ISI distribution (see both panels in Figure 5.2). Beyond the relative refractory period, tonic-firing neurons typically show exponentially decreasing distributions, as in Figure 5.2a. Instead, spike trains structured as sequences of patterns often display more complex distributions. Figure 5.2b shows a distribution with two prominent peaks. The first one accounts for the intervals between successive spikes belonging to the same burst, whereas the second one represents the typical interval between the last spike of a burst, and the first spike of the next burst. Burst firing, therefore, leaves a clear footprint on the ISI distribution.

Spike trains generated by complex dynamical processes produce multimodal distributions. However, the converse is not always true: a multimodal  $P(\Delta t)$  does not guarantee that the spiking dynamics is not Poissonian. Indeed, a Poisson process driven with a time-dependent signal may give rise to a multimodal distribution. Therefore, it is also useful to explore higher-order statistical properties of the spike train, as in the next section.

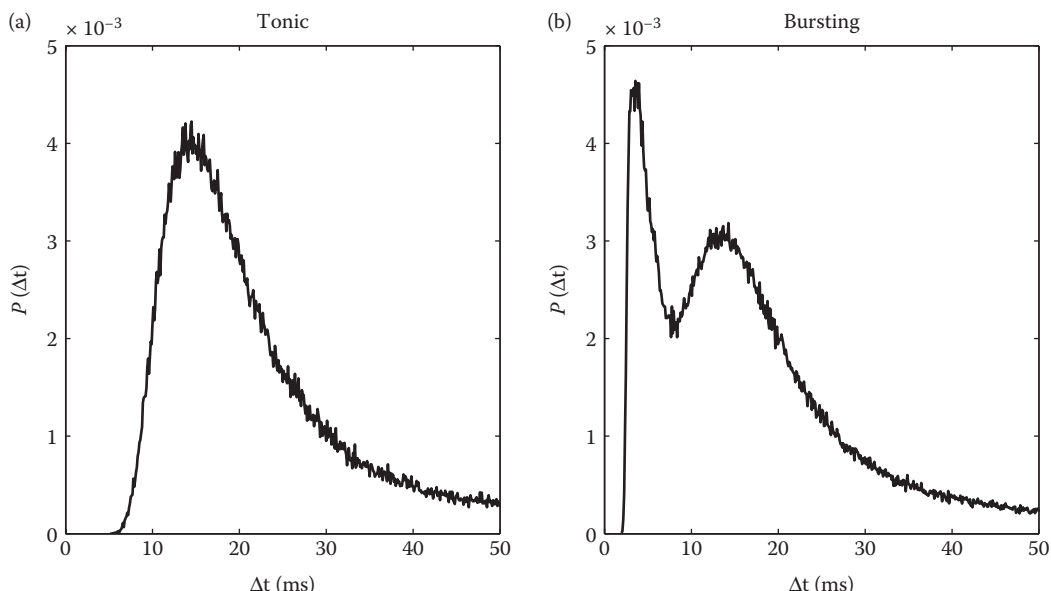


**FIGURE 5.2** Inter-spike interval (ISI) probability distributions for tonic and bursting responses. Intervals below 3 ms are not present due to the refractory period. A peak ISI is then followed by either an exponentially decreasing tail (a) or a second peak (b). For (b), the first peak results from spikes occurring within bursts whilst the second peak describes the larger separation between tonic spikes. The most probable ISIs in (a) (between 15 and 18 ms) correspond to the time scales of the second peak in (b).

### 5.3.3 AUTOCORRELATION FUNCTION AND FANO FACTOR

Second-order statistics can capture more structure in the spike train than the ISI distribution, and thus reveal more features of the underlying patterns. Figure 5.3 shows a representative example where the presence of bursts in the spike train is clearly identifiable from the autocorrelation function.

Typically, the correlation structure in spike trains results from both intrinsic interactions between spikes and overall signal modulations of the response (Panzeri and Schultz, 2001). In order to compute an autocorrelation that only shows the contribution of the within-trial interactions, a multi-trial recording is needed, that is, the response of the neuron to repeated presentations of the same time-dependent stimulus. For each trial, the spike train is binned at a given resolution  $\Delta t$  (0.25 ms, in the case of Figure 5.2). The binned spike trains are used to construct a binary response function  $n^\alpha(t)$ , where  $\alpha$  labels one specific trial, and  $t$  is the time since the start of the trial. Whenever there is a spike in the time bin corresponding to time  $t$ , we set  $n^\alpha(t) = 1$ , otherwise  $n^\alpha(t) = 0$ . We then compute the corrected autocorrelogram  $C(\tau)$  as

$$C(\tau) = \left\langle \frac{\langle n^\alpha(t)n^\alpha(t+\tau) \rangle_t - \frac{1}{2} [\langle n^\alpha(t)n^{\alpha-1}(t+\tau) \rangle_t + \langle n^{\alpha-1}(t)n^\alpha(t+\tau) \rangle_t]}{\Delta t \langle n^\alpha(t) \rangle_t} \right\rangle_\alpha \quad (5.4)$$

The averages  $\langle \cdot \rangle_t$  and  $\langle \cdot \rangle_\alpha$  are taken over all possible time bins and trials, respectively. The first term in the numerator is the average of spike pairs separated by a time lag of  $\tau$  ms. The second term is called the symmetrized shift predictor and accounts for the average number of spike pairs,

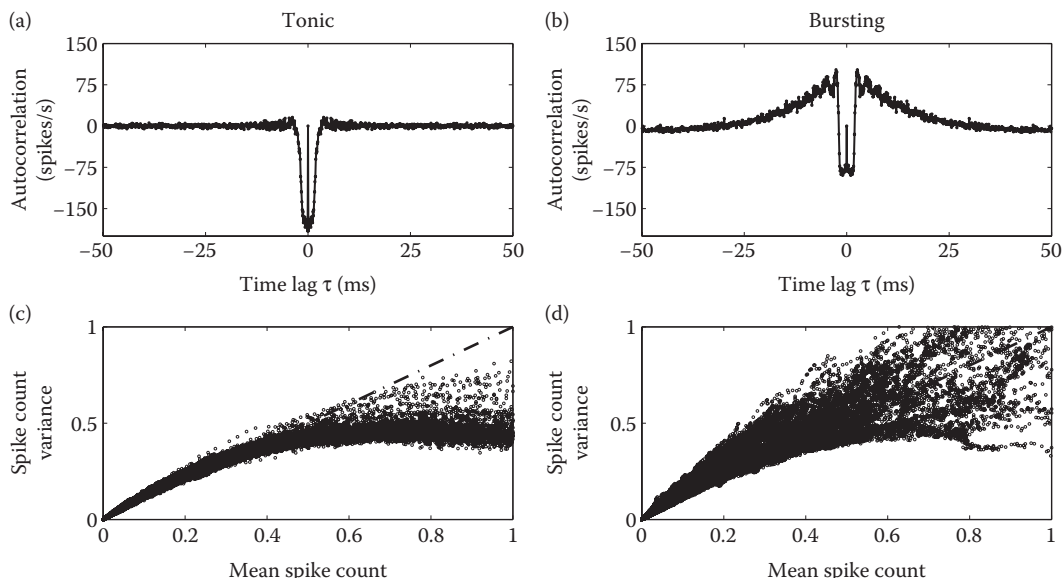


**FIGURE 5.3** Spike autocorrelation and reliability of bursting and tonic responses. Normalized autocorrelograms of tonic (a) and burst (b) responses. Negative area swept by the autocorrelation is attributed to the refractory period, while positive areas result from bursting. (c, d) Spike reliability measured as a Fano distribution of mean spike count and variance for tonic (c) and burst (d) responses. Poissonian responses are represented by dashed lines  $M(t) = V(t)$ . Correlation due to the refractory period limits the variance to below the Poissonian case while burst-related correlations increase this variance, producing super-Poissonian distributions.

separated by  $\tau$  ms, predicted to occur only as a consequence of spike rate modulations. Thus, in this form, the autocorrelation function only accounts for within-trial correlations. Signal correlations that are due to overall fluctuations in the spike rate are explicitly discarded.

Figure 5.3a shows the autocorrelation function computed on spike trains generated using a standard IF model, that is, by Equation 5.2 without the  $I_T$  current. The only evident structure is that spikes are negatively correlated at short times due to refractoriness. After a time lag of around 3 ms, spikes are uncorrelated. Figure 5.3b shows a typical corrected autocorrelogram obtained with a bursting neuron. The traces were computed using the full model of Equations 5.2 and 5.3. In addition to the negative correlations due to refractoriness, now the spike train exhibits large positive correlations at time scales of the order of burst duration.

Temporal correlations in the spike patterns can affect reliability across multiple presentation of the same stimulus. We can measure the spike count in response windows  $(t, t + T)$ , for  $t = 0, T, 2T, \dots$ . For each window starting at  $t$  the spike count  $n_i(t)$  is computed for every trial in each window  $t$ . From this, we can compute the mean  $n(t)$  and variance  $\sigma_n^2(t)$  of  $n_i(t)$  across trials. Then for each window, the Fano factor is defined as

$$F_T = \frac{\sigma_n^2(t)}{n(t)}. \quad (5.5)$$

For a pure Poisson process  $F_T(t)$  is equal to 1, apart from random fluctuations due to limited sampling (Gabbiani and Koch, 1998). Thus, systematic departures from unity contain information about correlations present in the spike train (Dayan and Abbott, 2001). The most obvious source of such correlations is the refractory period in neural firing. However, correlated spike patterns, like bursts, also affect the profile of Fano factors across different time windows. In general, the Fano factor can be related to the correlation function (Gabbiani and Koch, 1998; Panzeri et al., 1999). Positive correlations induce a Fano factor larger than unity, while negative correlations are reflected in a Fano factor smaller than 1. Figure 5.3c shows the Fano factor for the standard IF model. Due to the presence of negative correlations derived from the refractory period, the Fano factor is systematically smaller than one. Instead, Figure 5.3d shows that the positive correlations induced by bursts have a strong effect in a large number of time windows, rendering a Fano factor larger than unity. Although the dataset was used to produce Figure 5.3, which was simulated with a simple IFB model, the presence of bursts suffices to capture the distribution of Fano factors reported in experimental data of bursting neurons (Montemurro et al., 2007).

### 5.3.4 TUNING CURVES FOR SPIKE PATTERNS

The first characterizations of the code used by sensory neurons were presented in terms of tuning curves. Tuning curves relate a given stimulus feature to the intensity of the output signal. While the relevant stimulus feature can be any variable modulating neural activity, in general, the output variable is the firing rate (Dayan and Abbott, 2001). Choosing another aspect of neural output may highlight the relationship between the selected stimulus feature and the specific output. Here we construct tuning curves where the chosen response feature tags a specific type of spike pattern. As before, we focus on bursts.

There is evidence both experimental (DeBusk et al., 1997; Kamondi et al., 1998; Harris et al., 2002; Martinez-Conde et al., 2002; Cang and Isaacson, 2003; Arganda et al., 2007) and theoretical (Kepcs et al., 2002; Kepcs and Lisman, 2003; Samengo and Montemurro, 2010), suggesting that bursts may encode information by modulating their size as a function of specific stimulus characteristics. Hence, here we construct tuning curves relating different stimulus features with the length of bursts.

The first attempt in this direction was pioneered by Kepcs et al. (2002). They studied a two-compartment model of a pyramidal neuron (see Figure 5.4) driven by a fluctuating current.

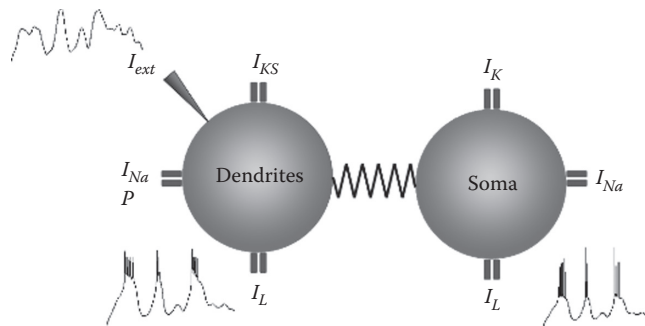


**FIGURE 5.4** Cortical neuron model. Schematic representation of the two-compartment model and the ionic currents involved. The stimulus is injected into the dendritic compartment. Next to each compartment we also show an example trace of the membrane potential during burst generation. The ionic currents associated with each compartment are also indicated. For details of the model see Samengo and Montemurro (2010).

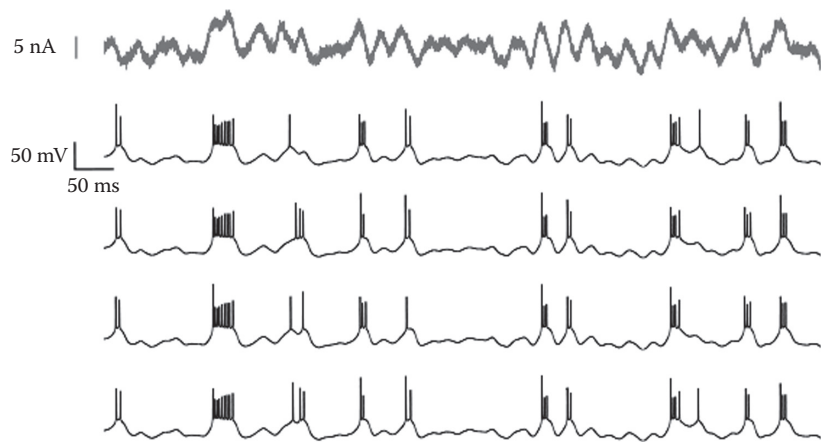


**FIGURE 5.5** Reproducibility of burst traces. Typical responses obtained for a random input current. The top trace represents a sample stochastic stimulus. The stimulus consists of a signal part (low-pass filtered Gaussian white noise with 10 Hz cut-off frequency), and a noise component (low-pass filtered Gaussian white noise with 1 kHz cut-off frequency, whose standard deviation (SD) is equal to 1/4 of the SD of the signal). The four example traces correspond to the output of the neuron when stimulated with the same signal component, and four different realizations of the noise. The numbers on top of the traces indicate the number of spikes in the bursts.

Figure 5.5 shows output traces from the model when the same current stimulus was presented 4 times, each with a different realization of an additional input noise current, added to introduce a certain degree of variability in the response. In spite of the presence of noise, the number of spikes per burst is largely preserved across trials. This reproducibility suggests that bursts are encoding information about the stimulus by modulating their size, and possibly their timing as well. The question of what bursts actually encode was systematically addressed by Kepes and Lisman for the first time (Kepes et al., 2002). By analyzing burst responses of a model cell when stimulated with a fluctuating current, they concluded that bursts encode the slope of the input signal.

In Figure 5.6, following Samengo and Montemurro (2010), we depict the response of the cortical model neuron to purely sinusoidal currents of different frequencies. Longer bursts tend to occur at earlier phases, higher amplitudes and smaller slopes of the input current (gray dots). One may therefore wonder which is the stimulus feature encoded by burst length: slopes, amplitudes, or phases?

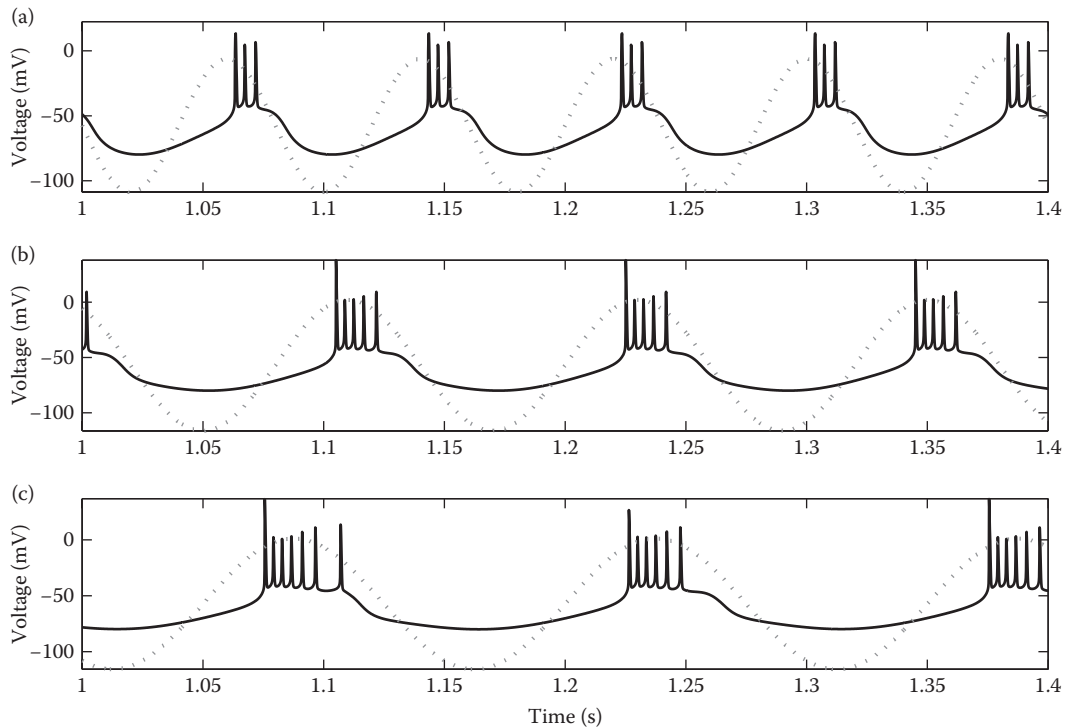


**FIGURE 5.6** Longer bursts occur earlier with respect to a sinusoidal input. The neuron model was stimulated with a purely sinusoidal input of amplitude of 6 nA and different periods,  $T$ . (a)  $T = 150$  ms; (b)  $T = 100$  ms; (c)  $T = 80$  ms.

This question was analyzed systematically by Samengo and Montemurro (2010). The study was performed using the same neuron model of Figure 5.4. The main conclusion was that the length of bursts encode the angular phase of the net input signal to the neuron much more accurately than its slope. Figure 5.7a shows a series of burst tuning curves for the cortical neuron model corresponding to stimuli with different statistics. For each stimulus, a large number of bursting events were classified by their size and the angular phase of the stimulating current at the time of burst onset was calculated. The curves in Figure 5.7a show the angular mean (Fisher, 1993) of the input-current's phase at burst onset as a function of burst size. Different curves are obtained with stimuli of different cut-off frequency. The near superposition of the curves indicates that there is a tight relationship between the particular value of the phase of the input signal at burst onset and the number of spikes in the elicited burst. Interestingly, the relationship is robust and does not depend on the cut-off frequency of the stimulus. Figure 5.7b shows the relationship between the slope of the input signal at burst onset and the associated burst size. While for low cut-off frequencies there is a monotonic relationship between the variables, the correspondence breaks down at cut-off frequencies larger than 20 Hz. Moreover, the different curves are markedly distinct. Therefore, the input slope can only be decoded from the observation of burst size if explicit knowledge of the input cut-off frequency is available. There is no universal mapping between input slope and burst size. Phases are thus better represented than slopes. This conclusion is based on the analysis of the robustness of tuning curves while varying the statistical properties of the stochastic input current, as in this case, the cut-off frequency.

Recently, the phase of the local field potential (LFP) at the timing of spikes was demonstrated to contribute additional information to that carried by the spikes alone (Montemurro et al., 2008; Kayser et al., 2009). In order for the brain to be able to exploit this extra information, downstream

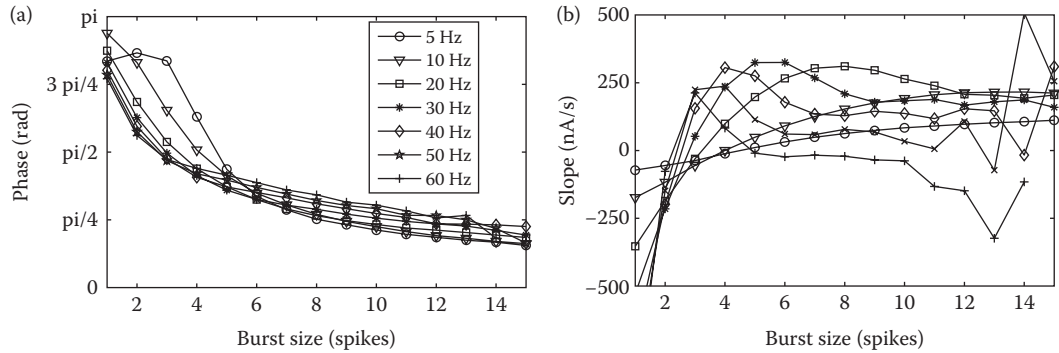


**FIGURE 5.7** Burst tuning curves. (a) Mean phase of the low-pass Gaussian stimulus at burst onset, as a function of the number of spikes per burst  $n$ . Different curves correspond to stimuli of different cut-off frequency. All curves collapse, indicating that all cut-off frequencies induce the same mapping between  $n$  and phase. The standard deviation of the stimulus is 3.6 nA. (b) Slope at burst onset for the same stimuli as in (a). Different cut-off frequencies induce different mappings between  $n$  and slope.

neurons need to know the value of the phase of the LFP at the location of the somas of their pre-synaptic afferents. Since the LFP is highly correlated with the total input arriving to a local brain area (Logothetis, 2003), the tight correspondence between burst length and input phase is an attractive candidate mechanism that can make the phase of the LFP explicitly available to downstream neurons.

### 5.3.5 EVENT TRIGGERED AVERAGES

In this section, we introduce the notion of event-triggered averages as generalizations of the concept of spike-triggered averages (STAs). As reviewed below, the STA provides an intuitive picture of the typical stimulus segment eliciting spikes. If the neural code is composed of sequences of patterns—and not just sequences of isolated spikes—one may also estimate the pattern-triggered average, one average for each type of pattern. If significant differences between the averages associated to different patterns are found, then different patterns have different meanings, in terms of the stimuli that generate them. The neural code is thus instrumented by several different code-words (patterns), representing distinct stimulus properties.

The STA is proportional to the correlation between the spike train  $\rho(t)$  and the stimulus  $I(t)$ . Specifically,

$$\text{STA}(t) = \frac{1}{N} \int_{-\infty}^{\infty} \rho(t) I(t' + t) dt' \quad (5.6)$$

By using Equation 5.1 the integral on the right-hand side of Equation 5.6 can be transformed into a sum over stimulus trajectories immediately preceding a spike event,

$$\text{STA}(t) = \frac{1}{N} \sum_{i=1}^N I(t_i + t) \quad (5.7)$$

The STA has been often interpreted as the typical stimulus trajectory that is most likely to elicit a spike (Rieke, 1997; Agüera y Arcas and Fairhall, 2003; Agüera y Arcas et al., 2003; Petersen et al., 2008).

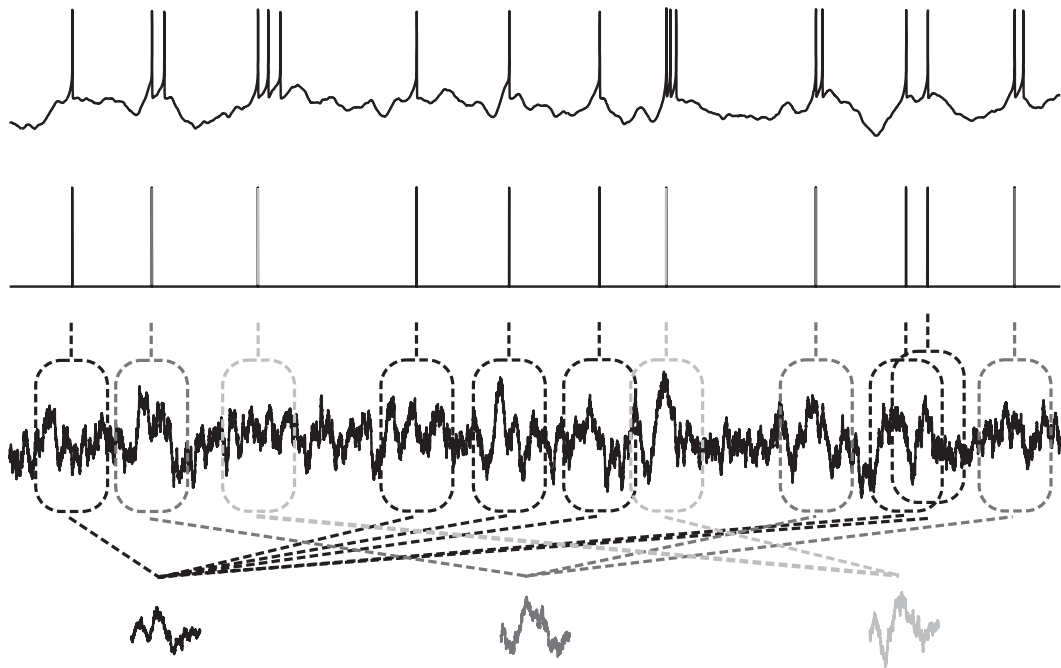


**FIGURE 5.8** Schematic representation of the burst triggered averages (BTAs). For each burst of a given size, all the stimulus trajectories leading up to burst onset are averaged according to Equation 5.8.

The idea behind the STA can be extended to any type of neural events, like bursts. In this case it is customary to refer to it as burst triggered average (BTA). We represent the sequence of bursts of a given size  $m$  by simply specifying the onset times of those events,  $B_m = \{t_j\}_{j=1}^K$ , where  $K$  represents the total number of events. Then, the BTA corresponding to bursts containing exactly  $m$  spikes can be written as

$$\text{BTA}_m(t) = \frac{1}{K} \sum_{j=1}^K I(t_j + t) \quad (5.8)$$

and a diagrammatic representation is shown in Figure 5.8.

The BTA can be used to disclose the specific stimulus characteristics that elicit each particular type of burst. As an example, in Figure 5.9 we show the BTAs of the IFB model described by Equations 5.2 and 5.3 when driven by an Ornstein–Uhlenbeck input current. We see systematic differences between the BTAs corresponding to bursts of different  $m$ . Specifically, longer bursts require deeper and more sustained hyperpolarization periods. Indeed, in thalamic relay cells the activation of the  $I_T$  current requires a sustained period of hyperpolarization (Sherman, 2001).

## 5.4 REVEALING INTRINSIC DYNAMICAL PROPERTIES

In its usual conception, spike-train analysis is useful to reveal the stimulus features that modulate the firing probability of a cell. Characterizing these features provides insight into the neural code. In the previous sections, we have applied these concepts to describe neural codes based on patterns of spikes. Less known, however, is the use of spike-train analysis as a tool to characterize intrinsic neural characteristics. In this section, we describe the way in which the STA is related to single-neuron dynamical properties.

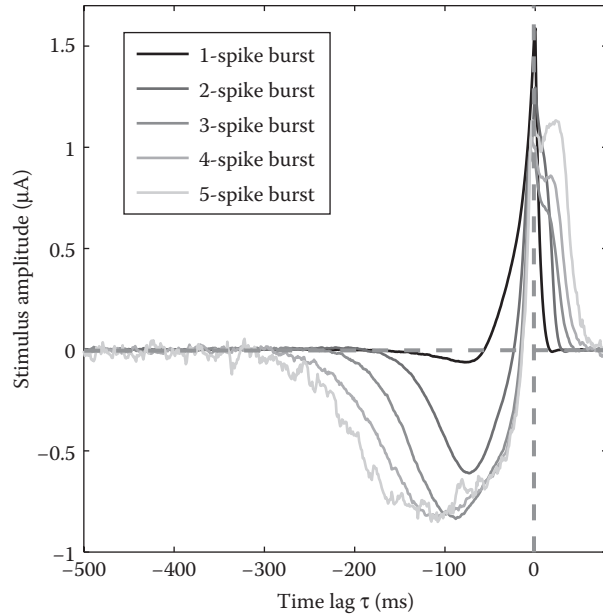


**FIGURE 5.9** Stimulus preferences of bursts in thalamic relay neurons. The BTAs reveal that bursts of different size are evoked by distinct stimulus features. Dashed lines indicate 0 for both axes. The first spike of the burst occurs at  $\tau = 0$  ms.

#### 5.4.1 NEURONS AS DYNAMICAL SYSTEMS

Mathematically, neurons are represented as dynamical systems. These systems are expressed as a set of differential equations describing the evolution of the membrane voltage and some other variables representing the internal state of ionic channels. For example, in the Hodgkin–Huxley model (Hodgkin and Huxley, 1952), the state of a neuron is described by the voltage  $V$ , the activation variables of sodium and potassium voltage-dependent channels ( $m$  and  $n$ ) and the inactivation of sodium channels ( $h$ ). These four variables define a vector in four-dimensional space, whose temporal evolution is described by four differential equations,

$$\begin{aligned} C \frac{dV}{dt} &= -g_L(V - V_L) - g_K n^4 (V - V_K) - g_{Na} m^3 h (V - V_{Na}) + I(t), \\ \frac{dm}{dt} &= -\frac{m - m_\infty(V)}{\tau_m(V)}, \\ \frac{dh}{dt} &= -\frac{h - h_\infty(V)}{\tau_h(V)}, \\ \frac{dn}{dt} &= -\frac{n - n_\infty(V)}{\tau_n(V)}, \end{aligned} \quad (5.9)$$

In the first equation,  $I(t)$  represents the external current. This current is the effective input to the neuron, arriving from the dendritic terminals, or from physical stimuli (light, sound, etc.) transduced into an electrical current by sensory receptors.

When  $I(t)$  is constant, the system (5.9) is autonomous, that is, it bears no explicit dependence on time. The behavior of such systems can be understood by analyzing the geometry of the

trajectories in phase space. When the external current surpasses a given threshold ( $9.8 \mu\text{A}/\text{cm}^2$ , in the case of Hodgkin–Huxley), all trajectories converge to a limit cycle. This cycle forms a closed curve in 4-dimensional space. Repetitive revolution along the curve represents repetitive firing. A projection of the limit cycle on the plane defined by the variables  $V$  and  $m$  is shown in Figure 5.10a. When the voltage is displayed as a function of time (Figure 5.10b), the usual spiking traces are obtained.

There are many neural models, with varying complexity. Some models include tens or even hundreds of ionic variables, and also monitor the concentration of calcium or other regulatory particles that diffuse in the cellular cytoplasm. More abstract models only describe the membrane voltage, and a few other effective variables that represent the combined effect of several biophysical quantities. In all cases, however, repetitive firing is associated with the existence of a stable limit cycle, attracting nearby trajectories.

When the input current is below the firing threshold, there is no limit cycle. Hence, at threshold, the phase portrait of the system undergoes a major transformation: a stable limit cycle is created through a bifurcation. There are several types of bifurcations. One of the main conclusions of the dynamical studies of neurons (Rinzel, 1987; Izhikevich, 2007; Mato and Samengo, 2008) is that the coding properties of a cell operating near the firing threshold are crucially determined by the type of bifurcation associated to the creation of the limit cycle. Two well-studied prototypes are given by resonator and integrator neurons. In the former, the firing onset is governed by a Hopf bifurcation. Right above threshold, resonator neurons fire with a well-defined frequency, that is fairly independent of the magnitude of the external current. In Figure 5.11a, we see the firing rate of a Hodgkin–Huxley neuron, as a function of the external input.

When  $I(t)$  also contains small fluctuating perturbations, these neurons provide a all-or-none code: either they fire or they do not fire. When they do fire, there is little modulation of their frequency (see Figure 5.11a). These neurons act as frequency detectors: they are more likely to fire whenever the input current has significant power in the frequency band corresponding to the firing limit cycle (in the supra-threshold regime) or the spiral fixed point (in the sub-threshold regime). Therefore, for time-dependent  $I(t)$ , there is no longer a fixed voltage threshold. The contingency of whether to spike or not to spike also depends on the history of the voltage trace.

Integrator neurons, instead, are associated with a saddle node bifurcation on the invariant circle. They fire with a frequency that strongly depends on the magnitude of the input current. In Figure 5.11b, the firing rate of an integrator neuron is shown as a function of the external input. Integrator neurons have a well-defined threshold.

Resonator and integrator neurons respond differently to fluctuations in the external current. These differences are explored in the next section, within the phase description of neural models.

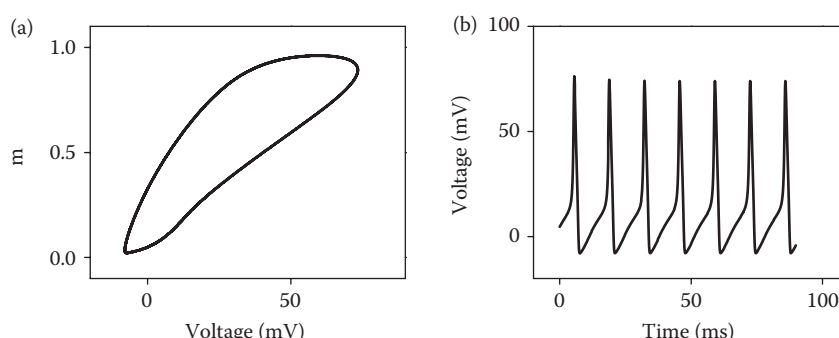


**FIGURE 5.10** Geometric representation of the Hodgkin–Huxley neuron model. (a) Projection of the four-dimensional phase space trajectory on the plane defined by the variables  $V$  and  $m$ . The closed orbit represents the firing limit cycle. (b) Temporal evolution of the voltage.

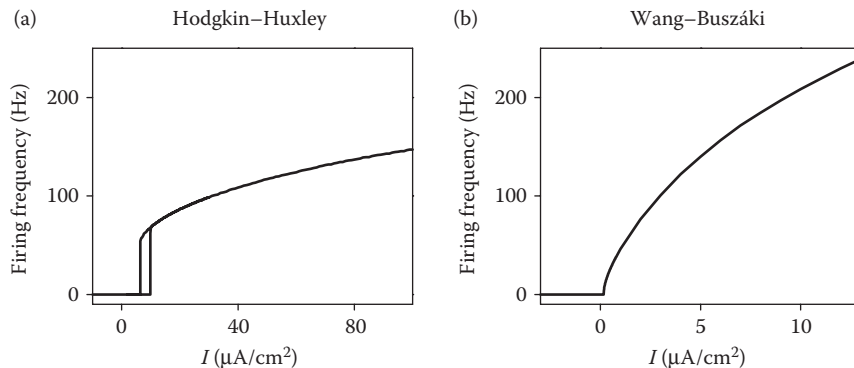


**FIGURE 5.11** Firing rate as a function of the magnitude of the constant input current. (a) Hodgkin–Huxley neuron model (resonator). There is a discontinuous jump of the frequency at the firing threshold. In the supra-threshold regime, the frequency varies little with the input current. (b) Wang–Buszaki neuron model (integrator). This model may be obtained from the Hodgkin–Huxley set of equations by modifying a few parameters (Wang and Buszaki, 1995). The frequency rises continuously from zero at the firing threshold, and varies significantly thereafter.

#### 5.4.2 PHASE-DESCRIPTION OF SPIKING NEURONS

In this section, we summarize the phase formalism of spiking dynamics. This formalism is useful in the cases when the modeled neuron is only slightly perturbed from the regularly spiking regime. For the moment, let us assume that the neuron is driven by a supra-threshold constant input current. Later on, we shall explore the effect of small fluctuating perturbations.

The dynamical system is circling around a limit cycle. The theory of phase reduction was introduced by Arthur Winfree (2001) and Kuramoto (1984). The main idea is to replace the original  $N$ -dimensional phase space by a 1-dimensional variable  $\varphi$  describing the state of the system. The variable measures the instantaneous location of the system on the limit cycle, and has units of phase. An increment of  $\varphi$  in  $2\pi$  represents a full turn on the limit cycle. The scale of  $\varphi$  along the cycle is chosen in such a way that it turns around with unit velocity:  $d\varphi/dt = 1$ . The origin  $\varphi = 0$  may be set anywhere on the limit cycle. For definiteness, we choose  $\varphi = 0$  as the point of maximal excursion of the voltage during spike generation. Hence, every time  $\varphi$  is an integer multiple of  $2\pi$ , we say a spike has been fired.

The theory of phase oscillators demonstrates that a small instantaneous perturbation in the input current either advances or delays the timing of the following spike. A small instantaneous perturbation produces a sudden increase of the voltage value of the neuron, leaving the remaining variables unchanged. This constitutes a small displacement away from the limit cycle. In Figure 5.12, the effect of the perturbation is illustrated.

When the neuron is displaced away from the limit cycle, it relaxes back. As it returns to the cycle, its phase may be either advanced or delayed, as compared with the unperturbed case. In a first-order description, the magnitude of the phase shift is proportional to the size of the perturbation. If several small perturbations are delivered within one turn around the limit cycle, the combined effect of them all is the sum of the effects of each individual perturbation (Kuramoto, 1984; Winfree, 2001). That is, the total phase shift is the sum of the individual phase shifts caused by each small perturbation. However, not all perturbations have the same effect. Some of them can produce large phase shifts, while others may be virtually ineffective. The crucial factor determining the effect of a perturbation is its timing. Perturbing the system during the spike has a different effect as perturbing it during the afterhyperpolarization phase, or during the repolarizing period before spike initiation.

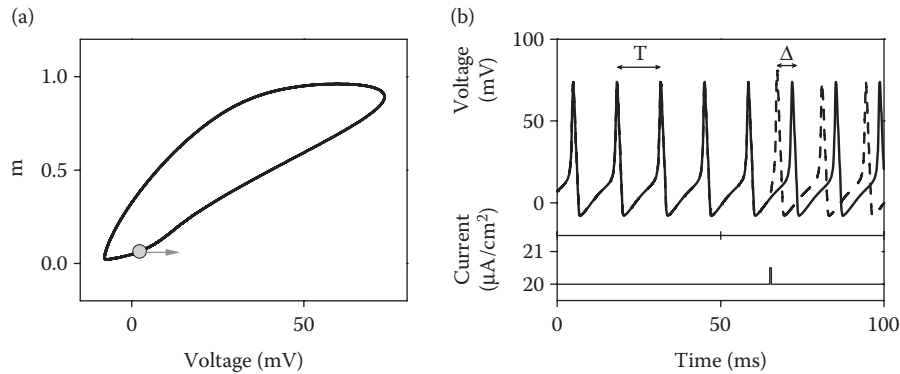


**FIGURE 5.12** The construction of phase-resetting curves. (a) A small current injection is delivered at time  $t_0$ , causing an advance or a delay in the timing of the following spike. The gray point represents the location of the system on the limit cycle, at time  $t_0$ . A positive, instantaneous current injection produces a sudden displacement of the voltage component to the right (gray arrow). (b) The instantaneous current injection is shown in the bottom panel. The upper panel compares the perturbed voltage trace (dashed line) with the unperturbed evolution (solid line). The first spike right after the perturbation typically comes at an advanced or delayed period, different from the original period  $T$ . The shift  $\Delta$  is defined as the difference between the timing of the unperturbed and perturbed spikes.

In order to administer instantaneous perturbations, we work with a constant input current that at time  $t_0$  jumps suddenly

$$I(t) = I_0 + I_1 \delta(t - t_0), \quad (5.10)$$

where  $\delta(x)$  represents Dirac delta function. The phase-response curve is defined as

$$\Delta(\theta, I_0) = \frac{2\pi}{T} \lim_{I_1 \rightarrow 0} \frac{\partial \Delta t(\theta, I_0, I_1)}{\partial I_1}, \quad (5.11)$$

where  $T$  is the period of the unperturbed oscillation,  $\Delta t(\theta, I_0, I_1)$  is the difference between the spiking times of the unperturbed and perturbed systems, and  $\theta$  is the phase at which the perturbation is introduced. This phase is simply related to the time  $t_0$  and the firing period  $T$ :  $\theta = 2\pi t_0/T$ . In what follows, we drop the explicit dependence of  $\Delta(\theta, I_0, I_1)$  on  $I_0$  and  $I_1$ , to simplify the notation. That is, from now on,  $\Delta(\theta) \equiv \Delta(\theta, I_0, I_1)$ .

With the definition of Equation 5.11, the linear theory of phase oscillators allows us to predict the evolution of the system in the presence of stochastic stimulation  $I(t) = I_0 + \sigma \xi(t)$ , where  $\xi(t)$  is Gaussian white noise of unit variance. This is,

$$\frac{d\phi}{dt} = 1 + \sigma \Delta(\phi) \xi(t). \quad (5.12)$$

If a spike was fired at  $t = 0$ , the following spike takes place at the time  $\tau$  required for  $\phi$  to reach  $2\pi$ . That is, when the equation

$$2\pi = \int_0^\tau [1 + \sigma \Delta(t) \xi(t)] dt \quad (5.13)$$

is fulfilled.

### 5.4.3 PHASE-RESPONSE CURVES OF RESONATOR AND INTEGRATOR NEURONS

Resonator and integrator neurons have qualitatively different phase-response curves. In resonator neurons, positive perturbations may either advance or delay spiking, depending on their timing. Spike anticipation produces a positive  $\Delta(\theta)$ , whereas a delay corresponds to a negative  $\Delta(\theta)$ . By alternating anticipations and delays, resonator neurons exhibit biphasic phase-response curves, with positive values of  $\Delta$  for some phases  $\theta$  and negative values for others (Figure 5.13a). In the case of the Hodgkin–Huxley model, delayed spiking is observed when the perturbation arrives before  $n$  has reached its minimum value, and  $h$  has reached its maximum. During regular spiking  $n$  is always fairly high (between 0.4 and 1) and  $h$  is always fairly low (between 0 and 0.4). Hence, a large fraction of the potassium channels are always open, and a considerable fraction of the sodium channels are always inactivated (notice that in Figure 5.13a, the dashed curves for  $n$  and  $h$  never cross). This makes spiking difficult. During the interval when  $n$  is still growing and  $h$  is still diminishing, a positive voltage increment cannot give rise to spiking, because sodium is still mostly inactivated and large amounts of potassium are still coming out of the cell. The only effect of the voltage increment is to reopen the potassium channels, producing a further hyperpolarization. During this period,  $\Delta(\theta)$  is negative. Once  $n$  and  $h$  are fully recovered, however, excitation accelerates the approach to threshold, producing a positive phase-resetting curve.

Integrator neurons, in contrast, have almost entirely unimodal and positive phase-resetting curves (Figure 5.4b). Positive current injections almost always accelerate spiking. In the case of the Wang–Buszaki model, during regular spiking  $n$  and  $h$  cross significantly, both of them essentially covering the full range between 0 and 1 (see the dashed curves in Figure 5.13b). In this model, hence, spiking is easy. The cell can generate action potentials even if  $n$  has not reached its minimum value, and  $h$  is not necessarily at its maximum. Full recovery is not required, since the two variables make large excursions, and compensate each other. Therefore, positive instantaneous current injections almost always have a depolarizing effect, approaching the cell to threshold, and thus accelerating spiking. The phase-response curve is hence almost always positive. Spiking is delayed only if perturbations arrive while the cell is generating an action potential. This is seen in Figure 5.13b as a very brief initial interval when  $\Delta(\theta)$  is negative. As soon as the spike is finished ( $V$  becomes negative,  $n$  has passed its maximum, and  $h$  has passed its minimum) any external perturbation anticipates firing.

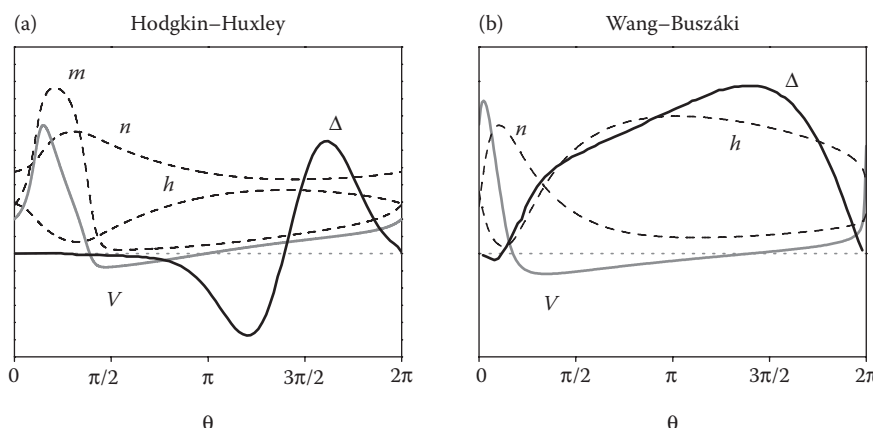


**FIGURE 5.13** Phase response curves. (a) Hodgkin–Huxley (resonator) neuron driven with  $I_0 = 20 \mu\text{A}/\text{cm}^2$ . (b) Wang–Buszaki (integrator) neuron driven with  $I_0 = 2 \mu\text{A}/\text{cm}^2$ . For comparison, the evolution of the variables ( $V, m, h, n$ ) is also included. Phase zero is defined as the moment when the voltage crosses a boundary of 20 mV from below. Resonator neurons have biphasic phase-response curves, whereas for integrator neurons  $F(\theta)$  is always positive.

The shape of a phase-resetting curve, therefore, is determined by the dynamical properties of the neuron. In other words, the shape of the function  $\Delta(\theta)$  reveals intrinsic cellular characteristics.

#### 5.4.4 RELATIONSHIP BETWEEN THE PHASE-RESPONSE CURVE AND THE STA: SUPRA-THRESHOLD REGIME

Bard Ermentrout et al. (2007) showed that the phase-resetting curve is the derivative of the negative STA. Here we present their derivation. They wrote the STA as an average of the time-dependent component of the stimulus  $\sigma\xi(t)$  around the spiking times  $\tau_j$

$$\text{STA}(t) = \sigma \langle \xi(\tau_j + t) \rangle_j \quad (5.14)$$

To that end, they calculated the spiking times  $\tau_j$  by expanding the spiking time  $\tau$  in Equation 5.13 in powers of  $\sigma$ . That is, they proposed

$$\tau = 2\pi + \tau_1\sigma + \tau_2\sigma^2 + \dots \quad (5.15)$$

Replacing this expansion in Equation 5.13 and keeping only the first order in  $\sigma$  yields

$$\tau_1 = - \int_0^{2\pi} \Delta(t) \xi(t) dt. \quad (5.16)$$

Hence,

$$\text{STA}(t) = \sigma \left\langle \xi \left[ 2\pi - \sigma \int_0^{2\pi} \Delta(t') \xi(t') dt' + t \right] \right\rangle_\xi. \quad (5.17)$$

The external noise  $\sigma$  is assumed to be small. Hence, in Equation 5.17,  $\xi$  is evaluated at times only slightly displaced from  $2\pi + t$ . This allows us to expand  $\xi(2\pi + t + \sigma\tau_1) \approx \xi(2\pi + t) + \sigma\tau_1\xi'(2\pi + t)$ . Replacing this expression in Equation 5.9, and noting that  $\langle \xi(2\pi + t) \rangle = 0$ , we get

$$\text{STA}(t) = -\sigma^2 \int_0^{2\pi} \Delta(t') \langle \xi(t') \xi'(2\pi + t) \rangle dt' = -\sigma^2 \int_0^{2\pi} \Delta(t') C'(2\pi + t - t') dt', \quad (5.18)$$

where  $C(s) = \langle \xi(t+s) \xi(t) \rangle_t$  is the correlation function of the injected noise. Integrating by parts, and noting that for Gaussian white noise  $C(s) = \delta(s)$ , we get

$$\text{STA}(t) = -\sigma^2 \Delta'(t). \quad (5.19)$$

Hence, the STA can be obtained from the phase-resetting curve, and vice versa.

#### 5.4.5 RELATIONSHIP BETWEEN THE PHASE-RESPONSE CURVE AND THE STA: SUB-THRESHOLD REGIME

If the mean stimulus  $I_0$  is below threshold, then the system no longer can be assumed to be orbiting regularly around the limit cycle (Equation 5.12). Hence, the state of the system cannot be described

in terms of a phase  $\varphi$ , and the concept of a phase-resetting curve is no longer applicable—though an analogous quantity will turn out to be useful, as shown below. We then turn to the description of the evolution of the voltage  $V$ . We begin with a linear-threshold neuron. In this model, the evolution of the membrane potential is governed by

$$V(t) = \sigma \int_{-\infty}^{+\infty} \Delta(t' - t) \xi(t') dt', \quad (5.20)$$

so that the voltage trace is a filtered version of the stimulus. Whenever the voltage crosses the threshold  $V_{\text{TH}}$  with a positive derivative, we say a spike has been fired. If the voltage is crossed when  $V$  is decreasing, nothing happens. This neuron model lacks resetting mechanisms. In Equation 5.20, the filter  $\Delta(t)$  plays an analogous role as in Equation 5.12: it weighs the effectiveness of stimulus fluctuations in modifying the state of the neuron. The only difference is that now  $\Delta(t)$  is not periodic, since there is no longer a limit cycle, nor a phase. Therefore, although it no longer represents a phase-resetting curve, it still captures the intrinsic integrating properties of the cell. Causality implies that  $\Delta(t)$  vanish for positive times, and limited memory imposes that  $\Delta(t) \rightarrow 0$ , when  $t \rightarrow -\infty$ . The simplest instance of Equation 5.20 is encountered in the example of Figure 5.14a, where  $\Delta(t) = e^t \Theta(-t)$ , and  $\Theta(t)$  is the Heaviside step function. This exponential filter is encountered when  $dV/dt = -V + \sigma \xi(t)$ . In Figure 5.14a, upward threshold crossings (i.e., spikes) are marked by arrows.

In the systems described by Equation 5.20, the STA reads (Fairhall et al., 2006; Hong et al., 2007)

$$\text{STA}(t) = V_{\text{TH}} \hat{\Delta}(t) - \sqrt{\frac{2}{\pi}} \sigma \hat{\Delta}'(t), \quad (5.21)$$

where  $\hat{\Delta}(t)$  and  $\hat{\Delta}'(t)$  are dimensionless versions of  $\Delta(t)$  and  $\Delta'(t)$ . Equation 5.21 implies that the STA is a linear combination of  $\Delta(t)$  and  $\Delta'(t)$ . The relative importance of  $\Delta(t)$  and  $\Delta'(t)$  is given by the ratio  $V_{\text{TH}}/\sigma$ . For low noise, or large threshold, the STA is proportional to  $\Delta(t)$ . In the opposite limit,  $V_{\text{TH}}/\sigma \ll 1$ , and the STA is similar to  $-\Delta'(t)$ . In this limit, we recover the result proved in the previous subsection.

In Figure 5.14c, we display several STAs corresponding to different values of the stimulus variance  $\sigma$ . The hollow symbols depict the limiting STAs predicted by Equation 5.21:  $V_{\text{TH}} \hat{\Delta}(t)$  when  $\sigma \approx 0$ , and  $-\sqrt{2/\pi} \sigma \hat{\Delta}'(t)$  when  $\sigma \rightarrow \infty$ . In this particular example  $\Delta(t)$  is an exponential function, multiplied by a step function. The derivative  $\Delta'(t)$  is composed of two terms: an exponential term, and a second term containing a delta function. We see that as  $\sigma$  varies, the STA ranges between the two predicted limits.

The simple integrator model of Equation 5.20 is restricted to filter-like neurons that lack resetting mechanisms after spike generation. In order to also consider resetting mechanisms, Omori et al. (2010) derived analytically the STA of a spike-response model including an afterhyperpolarization downstroke. They found that also in this case the STA is a linear combination of  $\Delta(t)$  and  $\Delta'(t)$ , though now with more complicated coefficients. On the right part of Figure 5.14, we display the STAs of a leaky IF model neuron. Figure 5.14b shows a typical voltage trace, where the resetting downstrokes following each spike are evident. In Figure 5.14d, the STAs corresponding to different noise levels are shown. Contrasting with the case of a pure integrator, we now see that even for large noise values the STA remains similar to  $\Delta(t)$ , with no visible contribution of  $\Delta'(t)$ . As the noise increases, the STA grows more rapidly, and becomes amplified. However, no evidence of a negative exponential term appears, nor a delta peak at zero. Equation 5.21, hence, does not describe the STA accurately. As argued by Fairhall and coworkers (2006), resetting mechanisms eliminate the possibility that the voltage crosses the threshold from above. Hence, the equation  $V(t) = V_{\text{TH}}$  suffices as

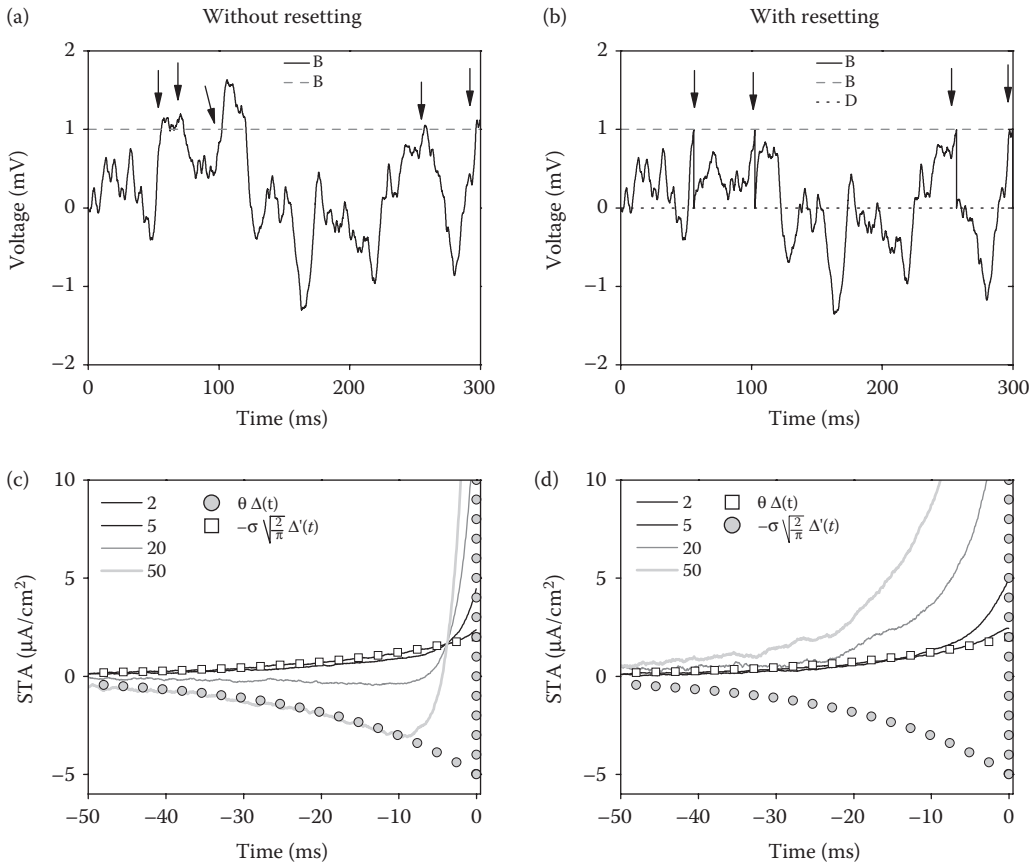


**FIGURE 5.14** Integrator neurons in the presence of noise. Left side: simple integrator model, described by Equation 5.21. Spikes are fired whenever the voltage reaches the threshold  $\theta = 1$ . Right side: leaky integrate-and-fire model. Spikes are fired at  $\theta = 1$ , and the voltage is immediately reset to  $V = 0$ . In both models,  $\Delta(t) = e^{t/\tau} \Theta(-t)/\tau$ ,  $\Delta'(t) = e^{t/\tau} \Theta(-t)/\tau^2 - e^{t/\tau} \delta(-t)/\tau$ , and  $\tau = 20$  ms. (a) and (b) Example voltage traces. Spikes are marked with arrows. (c) and (d) STAs corresponding to different noise levels. The hollow symbols depict the two limiting cases predicted by Equation 5.13, for  $\sigma \rightarrow 0$  and  $\sigma \rightarrow \infty$ . In the last case, the scaling of the curve is calculated with  $\sigma = 20$ .

a spiking condition, with no need to evaluate the sign of  $V'(t)$ . The spiking dynamics is thus fully controlled by  $V(t)$ , and the STA remains similar to  $\Delta(t)$ .

One may wonder whether these simple arguments are applicable to more realistic conductance-based models. In Figure 5.15, we depict the STA for the Hodgkin–Huxley (panel a) and the Wang–Buszaki (panel b) neurons. In both cases, no DC input component has been included ( $I = 0$ ) and the noise has been varied up to the maximum value permitted by the model. Conductance-based models cannot be driven with arbitrary large noise levels. Too large subthreshold fluctuations destroy the spikes themselves. In Figure 5.15 we see the STAs obtained for the relevant ranges of  $\sigma$ , in each model. In the HH neuron, the STA changes substantially as  $\sigma$  increases, the high- $\sigma$  curves resembling the negative derivative of the low- $\sigma$  cases. In contrast, in the WB neuron, the shape of the STA remains approximately the same, throughout the whole range of explored  $\sigma$  values. Only a global rescaling is observed.

In order to see whether the previous arguments are also applicable to the Hodgkin–Huxley and Wang–Buszaki models, we evaluate the predictive power of  $V(t)$  and  $V'(t)$  in anticipating spike generation. To that end, we construct the spike-triggered average of voltage traces  $V(t)$ , that is, the time-to-time average of the voltage in a window extending between 20 ms before spike initiation,

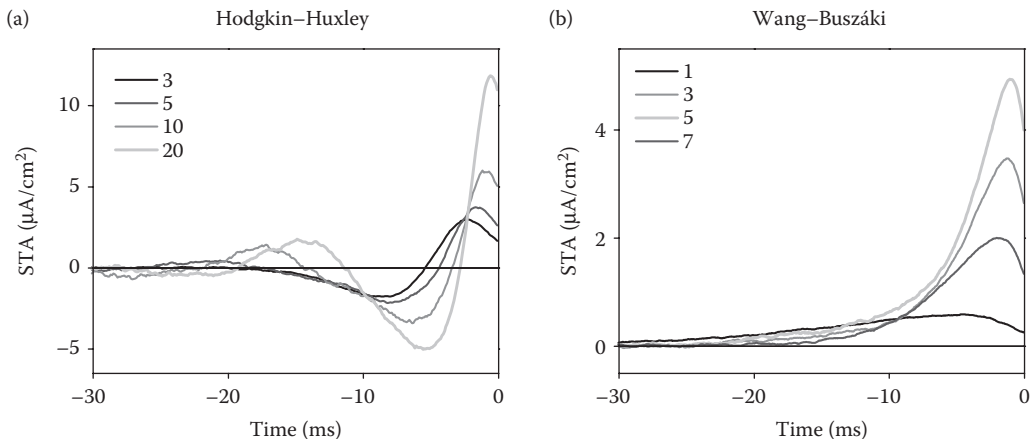


**FIGURE 5.15** STA of conductance-based models driven with  $I_0$  and several values of  $\sigma$ . In the legends,  $\sigma$  appears in units of  $\mu\text{A}/(\text{cm}^2 \text{ ms}^{1/2})$ . (a) Hodgkin–Huxley neuron model. (b) Wang–Buszaki neuron model.

and 10 ms after spike initiation. The result is shown in Figure 5.16a and b for the Hodgkin–Huxley and Wang–Buszaki models, respectively. We see that 10 ms before spike initiation, both models exhibit a considerable spread in their voltage values. However, about 5 ms before spiking, the voltage follows a fairly stereotyped trajectory, as judged from the small standard deviation of the average. Is the voltage value enough to predict that soon afterwards a spike will be generated? To answer this question, one must compare the distribution of voltage values prior to spike generation with the total distribution of voltage values, as shown in the insets. If the two distributions are markedly different, voltage is a good predictor of impending spiking. The same question may be asked with respect to the voltage derivative (Figure 5.16c and d).

In the insets of Figure 5.16, we see that both  $V(t)$  and  $V'(t)$  are good predictors of spike generation: the gray (prior) distributions are noticeably wider than the black ones (preceding spiking). However, a quantitative discriminability analysis shows that spiking in the Hodgkin–Huxley model is better predicted by the voltage derivative  $V'(x)$  than by the actual voltage value  $V(x)$ , for any time  $x$  in the window  $(-5, 0)$  ms. In Figure 5.16, if we compare the insets of panels (a) and (c), we see that the distribution of the derivative of the voltage is relatively sharper than the distribution of the voltage values themselves, with no significant change in the mean values. The opposite result is obtained in the WB model; in this case, the voltage is a better predictor than the derivative. Although the distribution in the inset of panel (d) is relatively sharper than in (b), discrimination is still better in (b). Note that the mean voltage preceding spike generation is different from the prior mean (the two distributions in the inset of panel (b) are displaced from one another). The mean derivative, in contrast, shows no evident displacement.

In resonator neurons, the firing threshold is not a sharp concept (Gerstner and Kistler, 2002; Izhikevich, 2007). Indeed, in a Hodgkin–Huxley neuron, a stimulus perturbation may be insufficient to induce spiking when delivered slowly, but result effective when delivered rapidly. Hence, not only the voltage value  $V(t)$  is important to decide whether to spike or not to spike, the derivative  $V'(t)$  also plays a role. In this respect, the Hodgkin–Huxley neuron resembles the integrator neuron of Figure 5.14. The Wang–Buszaki model, as an integrator neuron, has a well-defined threshold  $V_{\text{TH}}$ . The comparison of the actual  $V(t)$  with  $V_{\text{TH}}$  is already a good indicator of future spiking, with no essential need to know  $V'(t)$ . In this sense, the Wang–Buszaki neurons resemble the integrate-and-fire neuron shown in Figure 5.14.

The examples discussed here associate a purely positive STA with integrator properties, where spiking is entirely determined by a voltage threshold  $V_{\text{TH}}$ . In contrast, in resonator neurons the STA contains one or more pronounced oscillations, and its shape changes gradually as the input variance is increased. A shift from  $\Delta(t)$  to  $\Delta'(t)$  is indicative of a spiking decision involving both  $V(t)$  and  $V'(t)$ .

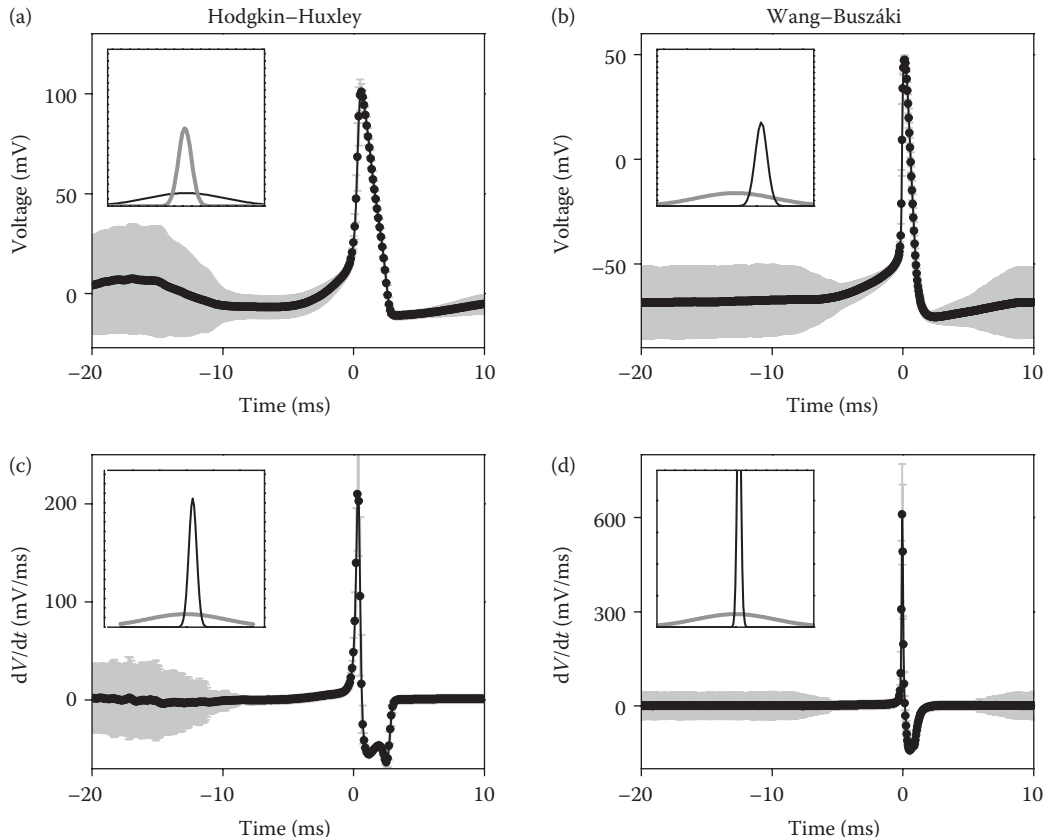


**FIGURE 5.16** Ability of the actual voltage  $V(t)$  and its derivative  $V'(t)$  in predicting future spikes. (a) and (b) Average voltage values surrounding spikes, for the Hodgkin–Huxley (a) and the Wang–Buszaki (b) models. The gray bars represent the standard deviation. (c) and (d) Same as in (a) and (b), but with the average voltage derivatives. Insets: Gaussian fit of the probability distribution of each voltage value (a) and (b) or voltage derivative (c) and (d). Gray line: prior distribution (not necessarily locked to spikes). Black line: only the values occurring 2 ms before spike generation are included. The result of the discriminability analysis does not vary, if  $V(t)$  and  $V'(t)$  are evaluated at some other time  $t_0$  between 0 and 5 ms preceding spike generation.

#### 5.4.6 BRIDGING THE TWO REGIMES

In Section 5.4.4, we showed that  $\text{STA}(t) \propto \Delta'(t)$ . In Section 5.4.5, we saw that as noise increases, resonator neurons switch from a regime where  $\text{STA}(t) \propto \Delta(t)$  to another regime where  $\text{STA}(t) \propto \Delta'(t)$ . Integrator neurons, instead, remain proportional to  $\Delta(t)$ . How can the two regimes be reconciled? Section 5.4.4 deals with the case where the neuron is spiking regularly, that is, the mean input current is high enough as to maintain the system on the limit cycle. The derivation that leads to Equation 5.13, however, assumes that the mean input current is equal to zero. If the reasoning is extended to the case  $I_0 \neq 0$ , the mathematical formulas become rather complicated. However, when  $I_0 \gg \sigma$ , they become tractable again. In this limit,

$$\text{STA}(t) = V_{\text{TH}} \hat{\Delta}(t) - I_0 \hat{\Delta}'(t). \quad (5.22)$$

Hence, in the limit of very large  $I_0$ , the two approaches give the same prediction.

## SUMMARY

In the first part of this chapter, we have shown how spike-train analysis methods can be used to establish the relationship between stimulus and response. In particular, we focused on basic techniques aiming at disclosing the presence and role of patterns in the neural response, addressing specifically the case of burst firing. In the second part, we showed how those techniques can be extended to reveal the dynamical properties of neurons regulating spike generation.

As our understanding of the richness and complexity of the neural code progresses, the integration and extension of different techniques and methods becomes more important. Here, we have brought together some of the basic tools that are required to unveil the relationship between stimulus and response based on the properties of the externally recorded neural output.

## REFERENCES

- Agüera y Arcas B, Fairhall AL. 2003. What causes a neuron to spike? *Neural Comput* 15:1789–1807.
- Agüera y Arcas B, Fairhall AL, Bialek W. 2003. Computation in a single neuron: Hodgkin and Huxley revisited. *Neural Comput* 15:1715–1749.
- Arfken GB, Weber H-J. 2005. *Mathematical Methods for Physicists*. Boston: Elsevier.
- Arganda S, Guantes R, de Polavieja GG. 2007. Sodium pumps adapt spike bursting to stimulus statistics. *Nat Neurosci* 10:1467–1473.
- Averbeck BB, Latham PE, Pouget A. 2006. Neural correlations, population coding and computation. *Nat Rev Neurosci* 7:358–366.
- Cang J, Isaacson JS. 2003. *In vivo* whole-cell recording of odor-evoked synaptic transmission in the rat olfactory bulb. *J Neurosci* 23:4108–4116.
- Dayan P, Abbott LF. 2001. *Theoretical Neuroscience: Computational and Mathematical Modeling of Neural Systems*. Cambridge, MA: Massachusetts Institute of Technology Press.
- DeBusk BC, DeBruyn EJ, Snider RK, Kabara JF, Bonds AB. 1997. Stimulus-dependent modulation of spike burst length in cat striate cortical cells. *J Neurophysiol* 78:199–213.
- Ermentrout GB, Galan RF, Urban NN. 2007. Relating neural dynamics to neural coding. *Phys Rev Lett* 99:248103.
- Eyherabide HG, Samengo I. 2010a. The information transmitted by spike patterns in single neurons. *J Physiol Paris* 104:147–155.
- Eyherabide HG, Samengo I. 2010b. Time and category information in pattern-based codes. *Front Comput Neurosci* 4:145.
- Fairhall AL, Burlingame CA, Narasimhan R, Harris RA, Puchalla JL, Berry MJ., 2nd. 2006. Selectivity for multiple stimulus features in retinal ganglion cells. *J Neurophysiol* 96:2724–2738.
- Fellous JM, Tiesinga PH, Thomas PJ, Sejnowski TJ. 2004. Discovering spike patterns in neuronal responses. *J Neurosci* 24:2989–3001.
- Fisher NI. 1993. *Statistical Analysis of Circular Data*. Cambridge, England: Cambridge University Press.
- Gabbiani F, Koch C. 1998. Principles of spike train analysis. In: *Methods in Neural Modeling*, pp. 313–360.
- Gardiner CW. 2009. *Stochastic Methods: A Handbook for the Natural and Social Sciences*. Berlin: Springer.
- Gaudry KS, Reinagel P. 2008. Information measure for analyzing specific spiking patterns and applications to LGN bursts. *Network* 19:69–94.
- Gerstner W, Kistler WM. 2002. *Spiking Neuron Models: Single Neurons, Populations, Plasticity*. Cambridge, UK: Cambridge University Press.
- Gütig R, Sompolinsky H. 2006. The tempotron: A neuron that learns spike timing-based decisions. *Nat Neurosci* 9:420–428.
- Harris KD, Henze DA, Hirase H, Leinekugel X, Dragoi G, Czurko A, Buzsaki G. 2002. Spike train dynamics predicts theta-related phase precession in hippocampal pyramidal cells. *Nature* 417:738–741.
- Hodgkin AL, Huxley AF. 1952. A quantitative description of membrane current and its application to conduction and excitation in nerve. *J Physiol* 117:500–544.
- Hong S, Agüera y Arcas B, Fairhall AL. 2007. Single neuron computation: From dynamical system to feature detector. *Neural Comput* 19:3133–3172.
- Izhikevich EM. 2007. *Dynamical Systems in Neuroscience: The Geometry of Excitability and Bursting*. Cambridge, MA: MIT Press.

- Kamondi A, Acsady L, Wang XJ, Buzsáki G. 1998. Theta oscillations in somata and dendrites of hippocampal pyramidal cells *in vivo*: Activity-dependent phase-precession of action potentials. *Hippocampus* 8:244–261.
- Kayser C, Montemurro MA, Logothetis NK, Panzeri S. 2009. Spike-phase coding boosts and stabilizes information carried by spatial and temporal spike patterns. *Neuron* 61:597–608.
- Kepecs A, Lisman J. 2003. Information encoding and computation with spikes and bursts. *Network* 14:103–118.
- Kepecs A, Wang XJ, Lisman J. 2002. Bursting neurons signal input slope. *J Neurosci* 22:9053–9062.
- Kuramoto Y. 1984. *Chemical Oscillations, Waves, and Turbulence*. Berlin: Springer-Verlag.
- Logothetis NK. 2003. The underpinnings of the BOLD functional magnetic resonance imaging signal. *J Neurosci* 23:3963–3971.
- Martinez-Conde S, Macknik SL, Hubel DH. 2002. The function of bursts of spikes during visual fixation in the awake primate lateral geniculate nucleus and primary visual cortex. *Proc Natl Acad Sci USA* 99:13920–13925.
- Mato G, Samengo I. 2008. Type I and type II neuron models are selectively driven by differential stimulus features. *Neural Comput* 20:2418–2440.
- Montemurro MA, Panzeri S, Maravall M, Alenda A, Bale MR, Brambilla M, Petersen RS. 2007. Role of precise spike timing in coding of dynamic vibrissa stimuli in somatosensory thalamus. *J Neurophysiol* 98:1871–1882.
- Montemurro MA, Rasch MJ, Murayama Y, Logothetis NK, Panzeri S. 2008. Phase-of-firing coding of natural visual stimuli in primary visual cortex. *Curr Biol* 18:375–380.
- Nadasdy Z. 2000. Spike sequences and their consequences. *J Physiol Paris* 94:505–524.
- Nelken I, Chechik G, Mrsic-Flogel TD, King AJ, Schnupp JW. 2005. Encoding stimulus information by spike numbers and mean response time in primary auditory cortex. *J Comput Neurosci* 19:199–221.
- Panzeri S, Schultz SR. 2001. A unified approach to the study of temporal, correlational, and rate coding. *Neural Comput* 13:1311–1349.
- Panzeri S, Schultz SR, Treves A, Rolls ET. 1999. Correlations and the encoding of information in the nervous system. *Proc Biol Sci* 266:1001–1012.
- Petersen RS, Brambilla M, Bale MR, Alenda A, Panzeri S, Montemurro MA, Maravall M. 2008. Diverse and temporally precise kinetic feature selectivity in the VPm thalamic nucleus. *Neuron* 60:890–903.
- Rieke F. 1997. *Spikes: Exploring the Neural Code*. Cambridge, MA: MIT Press.
- Rinzel J. 1987. A formal classification of bursting mechanisms in excitable systems. In: *Mathematical Topics in Population Biology; Morphogenesis; and Neurosciences*, Vol. 71 (Teramoto, E. and Yamaguti, M., eds), pp 267–281, Berlin: Springer-Verlag.
- Samengo I, Montemurro MA. 2010. Conversion of phase information into a spike-count code by bursting neurons. *PLoS One* 5:e9669.
- Sherman SM. 2001. Tonic and burst firing: Dual modes of thalamocortical relay. *Trends Neurosci* 24:122–126.
- Smith GD, Cox CL, Sherman SM, Rinzel J. 2000. Fourier analysis of sinusoidally driven thalamocortical relay neurons and a minimal integrate-and-fire-or-burst model. *J Neurophysiol* 83:588–610.
- Winfree AT. 2001. *The Geometry of Biological Time*. New York: Springer.